Saturation effects in fluorescence correlation spectroscopy

Lloyd M. Davis, Guoqing Shen and David A. Ball

Center for Laser Applications, University of Tennessee Space Institute, Tullahoma, TN 37388

ABSTRACT

Fluorescence correlation spectroscopy (FCS) could provide a more useful tool for intracellular studies and biological sample characterization if measurement times could be reduced. While an increase in laser power can enable an autocorrelation function (ACF) with adequate signal-to-noise to be acquired within a shorter measurement time, excitation saturation then leads to distortion of the ACF and systematic errors in the measurement results. An empirical method for achieving reduced systematic errors by employing a fitting function with an additional adjustable parameter has been previously introduced for two-photon FCS. Here we provide a unified physical explanation of excitation saturation effects for the three cases of continuous-wave, pulsed one-photon excitation, and two-photon excitation FCS. When the time between laser pulses is longer than the fluorescence lifetime, the signal rate at which excitation saturation occurs is lower for pulsed excitation than for cw excitation, and due to the disparate timescales of the photophysical processes following excitation, it is lower still for two-photon excitation. We use a single-molecule description of FCS to obtain improved analytical ACF fitting functions for the three cases. The fitting functions more accurately account for saturation effects than those previously employed without the need for an additional empirical parameter. Use of these fitting functions removes systematic errors and enables measurements to be acquired more quickly by use of higher laser powers. Increase of background, triplet photophysics, and the cases of scanning FCS and fluorescence cross-correlation spectroscopy are also discussed. Experimental results acquired with a custom built apparatus are presented.

1. INTRODUCTION

Fluorescence correlation spectroscopy (FCS) is an increasingly popular method for determining species concentrations and diffusion coefficients of labeled components within biological samples [1]. For applications such as high throughput screening and intra-cellular studies with limited observation times, there is a need to make measurements with reduced data acquisition times [2]. In order to obtain adequate photon statistics and signal-to-noise for short measurement durations, it is desirable to increase the photon count rate by increasing the laser power. However, as the laser power is increased, saturation and other effects cause the autocorrelation function (ACF) to change in amplitude and shape [3,4]. A modified fitting function has previously been introduced to account for saturation in ACF data collected at high laser powers in 2-photon excitation experiments [5,6]. However, this fitting function is obtained with the assumption that saturation has an abrupt onset and causes the probe region to have a flat-top shape. The assumed shape "has no physical meaning and introduces fictitious parameters" [7]. The fitting function includes an additional quantity (α), which is essentially an empirical parameter that lends added flexibility for better fitting of the saturation-distorted ACF data. Rate equation models of the molecular population dynamics have been previously used in attempts to provide a better physical understanding of saturation in FCS with two-photon excitation and in fluorescence experiments in general [3,8]. However, Ref. [3] only considers continuous-wave (cw) excitation, Ref. [8] assumes complete ground-state repopulation between laser pulses, and neither presents fitting of the ACF with saturation. Below we discuss the physical processes that occur following excitation of a fluorescent molecule and we present rate equation models to give a unified explanation of saturation effects for cw excitation, pulsed one-photon excitation, and two-photon excitation. Power series expansions of the fluorescence dependence on irradiance for each case are then used with a single-molecule derivation of the ACF to obtain improved fitting functions for FCS when saturation occurs.

2. GENERAL SATURATION CHARACTERISTICS

For one-photon excitation, either a cw laser beam or a train of sub-nanosecond pulses is used for sample excitation. However, for two-photon excitation, a train of pulses of duration ~100 femtosecond is usually used in order to attain adequate peak irradiance. The different timescales of the laser pulses and the physical processes that occur as a result of molecular excitation, which are indicated in Fig. 1 (a), give rise to different saturation behavior for one- and two-photon excitation and for pulsed and cw excitation.

Multiphoton Microscopy in the Biomedical Sciences V, edited by Ammasi Periasamy, Peter T. C. So, Proceedings of SPIE Vol. 5700 (SPIE, Bellingham, WA, 2005)
1605-7422/05/$15 · doi: 10.1117/12.591099

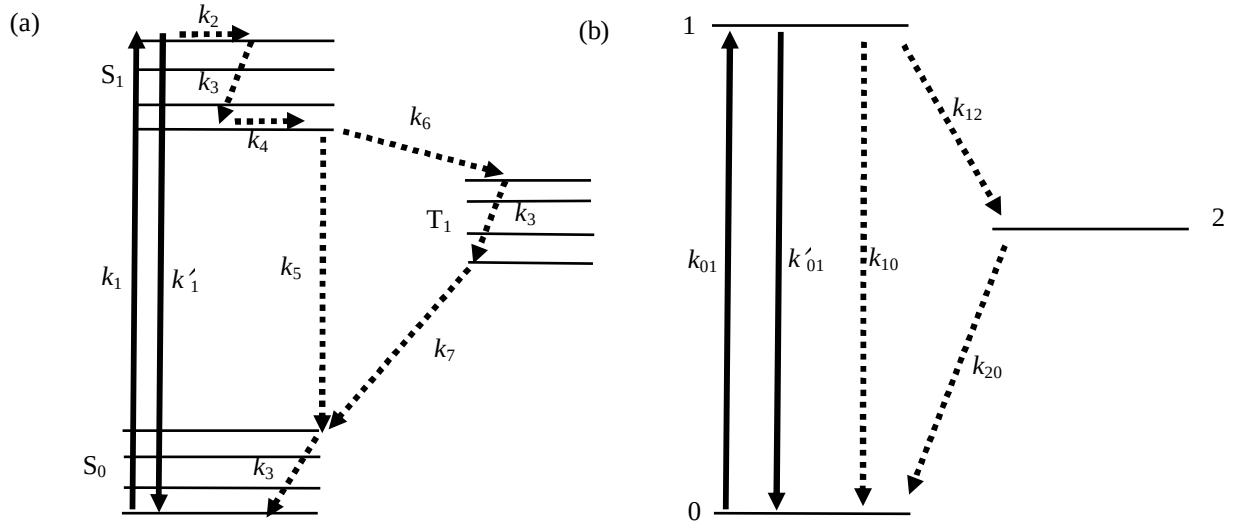

Fig. 1: (a) Typical timescales of molecular processes: k_1: one or two-photon excitation; k'_1: one or two-photon stimulated emission; k_2: collisional dephasing (~10 fs); k_3: vibrational thermalization (~1 ps); k_4: rotational reorientation (~100 ps—100 ns); k_5: fluorescence (~2 ns); k_6: inter-system crossing (~200 ns); k_7: phosphorescence (~1 μs); (b) Simplified 3-level scheme, in which only the electronic levels are retained.

After an organic dye molecule is excited (at a rate k_1 shown in Fig. 1 (a)) to a particular sublevel of the S_1 manifold, its electronic wavefunction becomes dephased due to elastic collisions with solvent molecules within a timescale of k_2^{-1}~10 fs, which is typically much faster than the laser excitation pulsewidth, and hence coherence effects are usually negligible and the optical Bloch equations that describe the system are well approximated by rate equations. After dephasing, thermal relaxation within the S_1 manifold due to inelastic collisions with solvent molecules occurs within a timescale of k_3^{-1}~1 ps. Reorientation of the transition dipole moment due to rotational diffusion of the molecule may also occur on a timescale of k_4^{-1}~100 ps for a small dye molecule in aqueous solution and with k_4^{-1} up to ~100 ns for a chromophore rigidly bound to a macromolecule. Fluorescence and/or internal conversion back to the S_0 manifold then occur within about k_5^{-1}~2 ns. A competing process, which typically occurs about 1 in 100 times, and thus with k_6^{-1}~200 ns, is intersystem crossing to the triplet T_1 manifold. In typical oxygen-saturated aqueous solutions, relaxation from T_1 back to the S_0 manifold then occurs within about k_7^{-1}~1 μs. Because of the disparate timescales of the molecular processes described above, the molecular energy level system in Fig 1 (a) is well approximated by the 3-level system shown in Fig. 1 (b), with $k_1 \rightarrow k_{01}$, $k'_1 \rightarrow k'_{01}$, $k_5 \rightarrow k_{10}$, $k_6 \rightarrow k_{12}$, $k_7 \rightarrow k_{20}$.

For cw excitation, saturation occurs primarily as a result of the decrease in the fractional population N_0/N of the ground state 0 with increasing laser intensity. The laser pumps molecules from the ground state 0 to the excited singlet state 1, but the stimulated emission pumping from 1 to 0, k'_{01} is negligible, because $k_3 >> k_1$ in Fig. 1 (a). The rate equations for the 3-level system may then be expressed as

$$\frac{d}{dt}\begin{pmatrix} N_0 \\ N_1 \\ N_2 \end{pmatrix} = \begin{pmatrix} -k_{01} & k_{10} & k_{20} \\ k_{01} & -k_{10}-k_{12} & 0 \\ 0 & k_{12} & -k_{20} \end{pmatrix}\begin{pmatrix} N_0 \\ N_1 \\ N_2 \end{pmatrix}, \tag{1}$$

which has the steady state solution

$$\begin{pmatrix} N_0 \\ N_1 \\ N_2 \end{pmatrix} = \begin{pmatrix} k_{10}+k_{12} \\ k_{01} \\ k_{01}k_{12}/k_{20} \end{pmatrix} \times \frac{N}{k_{10}+k_{12}+k_{01}(1+k_{12}/k_{20})}, \tag{2}$$

where N_j / N is the fractional population of level j, with $N = \sum N_j$. Here, the cw excitation rate is

$$k_{01} = \sigma_a \langle I \rangle / E_\gamma, \tag{3}$$

where σ_a is the absorption cross-section (equal to 3.82×10^{-21} cm^3 M times the molar absorptivity), $\langle I \rangle$ is the cw laser irradiance, and $E_\gamma = hc/\lambda_0$ is the laser photon energy, in which h is Planck's constant, c is the speed of light, and λ_0 is the vacuum wavelength of the laser. The mean fluorescence count rate from a single molecule, which is proportional to the decay rate k_{10}, and the fractional excited state population N_1/N, obtained from the second line of Eqn. (2), is given by

$$F = \frac{Ck_{10}}{1+Q}\frac{\langle I \rangle / I_S}{1+\langle I \rangle / I_S}, \tag{4}$$

where C is equal to the net collection and detection efficiency, the saturation intensity I_S is given by

$$I_S = 1/[\eta(1+Q)], \tag{5}$$

where η is defined by

$$\eta = \sigma_a \tau_F / E_\gamma, \tag{6}$$

$$\tau_F = (k_{10} + k_{12})^{-1} \tag{7}$$

is equal to the fluorescence lifetime, and

$$Q = R\tau_P / \tau_F, \tag{8}$$

in which $R = k_{12}/(k_{12}+k_{10})$ is the triplet crossing yield and $\tau_P = k_{20}^{-1}$ is the phosphorescence lifetime.

For repetitively pulsed excitation, ground state depletion during the course of each laser excitation pulse is a major factor that contributes to saturation. With the assumption that the duration of the laser pulse δt is short compared to the fluorescence lifetime ($\delta t << \tau_F$), the decay of the excited state and triplet populations during the interval of the laser pulse $0 < t < \delta t$ can be ignored, and the top line of Eqn. (1) gives

$$dN_0/dt = -k_{01}N_0 \ , \qquad \text{(during pulse)} \tag{9}$$

which has the solution

$$N_0(\delta t) = N_0(0)\exp(-k_{01}\delta t), \qquad \text{(for } \delta t << \tau_F\text{)} \tag{10}$$

with

$$k_{01} = \sigma_a \bar{I} / E_\gamma, \tag{11}$$

where for simplicity, the irradiance during the laser pulse is approximated to be the constant value $\bar{I}$. However, when the laser excitation pulsewidth is shorter than k_3^{-1}~1 ps, as it typically is for two-photon excitation, the laser not only excites the molecule, but for high irradiance it can drive the excited molecule back to the ground state by stimulated emission (as indicated in Fig. 1(b) by the downward transition at rate k'_{01}), so that Eqn. (9) should be replaced by

$$dN_0/dt = -k_{01}N_0 + k'_{01}N_1 \qquad \text{(during pulse).} \tag{12}$$

The time after excitation until the next laser pulse, T, is much greater than the time required for thermalization of the excited state manifold k_3^{-1}~1 ps and hence in Eqn. (12) $N_1(0)\approx0$, so that the solution of Eqn. (12) is

$$N_0(\delta t) = N_0(0)\left(1+\exp(-2k_{01}\delta t)\right)/2 \ , \qquad \text{(for } \delta t << k_3^{-1}\text{)}, \tag{13}$$

where we have assumed that $k'_{01} = k_{01}$, which will be the case if there is no difference in the degeneracy or density of levels in the S_0 and S_1 manifolds. For two-photon excitation, Eqn. (11) is replaced by

$$k_{01} = \sigma_{TPF}\bar{I}^2 / E_\gamma^2 \ , \tag{14}$$

in which σ_{TPF} is the two-photon absorption cross section, typically expressed in units of GM=10^{-50} cm^4 s. A comparison of Eqns. (10) and (13) shows that the width of the laser pulse (in comparison to the k_3^{-1}~1 ps time for thermalization of the S_1 manifold) can significantly alter the saturation behavior. Note that equation (14) is a classical approximation and σ_{TPF} should be regarded as an effective parameter for the particular detailed photon statistics (i.e., the second order quantum mechanical coherence function of the light), which will depend on the shape, chirp, and coherence of the pulse.

After the laser pulse, the molecule relaxes from the excited state 1. The solution of Eqn. (1) with k_{10}=0 can then be used with the initial condition of Eqn. (10) or (13) and the periodicity condition $N_j(T) = N_j(0)$, j = 0,1,2, to determine the dependence of the mean fluorescence count rate $F = \int_0^T F(t)dt/T$ on the average laser irradiance,

$$\langle I \rangle = \bar{I}\,\delta t / T \ . \tag{15}$$

For sub-nanosecond pulses, the solution of Eqn. (1) with the initial condition of Eqn. (10) yields

$$F = Ck_{10}\frac{\tau_F}{T}\left(1-e^{-T/\tau_F}\right)\frac{1-\exp\left(-\langle I \rangle / I_S'\right)}{1+Q-\exp\left(-\langle I \rangle / I_S'\right)\left(\exp(-T/\tau_F)+Q\right)} \tag{16}$$

$$\approx Ck_{10}\frac{\tau_F}{T}\frac{1-\exp\left(-\langle I\rangle/I_S'\right)}{1+Q-Q\exp\left(-\langle I\rangle/I_S'\right)}, \quad \text{for } \tau_F \ll T, \tag{17}$$

where

$$I_S' = (\eta T/\tau_F)^{-1}, \tag{18}$$

and

$$Q = R\frac{\tau_P}{\tau_P-\tau_F}\frac{e^{-T/\tau_P}-e^{-T/\tau_F}}{1-e^{-T/\tau_P}} \tag{19}$$

$$\approx R\frac{\tau_P}{T}, \quad \text{for } \tau_F \ll T \ll \tau_P\ . \tag{20}$$

For the typical values of $R \sim 10^{-2}$, $\tau_P \sim 1$ µs, $T \sim 10$ ns, Eqn. (20) gives $Q \sim 1$ and Eqn. (17) shows that near saturation triplet shelving reduces the mean fluorescence signal by ~50%. For sub-picosecond pulses, the solution of Eqn. (1) with the initial condition of Eqn. (13), and with Eqn. (11) for one-photon excitation yields

$$F = Ck_{10}\frac{\tau_F}{T}\left(1-e^{-T/\tau_F}\right)\frac{1-\exp\left(-2\langle I\rangle/I_S'\right)}{2+2Q-\left(1+\exp\left(-2\langle I\rangle/I_S'\right)\right)\left(\exp\left(-T/\tau_F\right)+Q\right)} \tag{21}$$

$$\approx Ck_{10}\frac{\tau_F}{T}\frac{1-\exp\left(-2\langle I\rangle/I_S'\right)}{2+Q-Q\exp\left(-2\langle I\rangle/I_S'\right)}, \quad \text{for } \tau_F \ll T, \tag{22}$$

whereas Eqn. (13) with Eqn. (14) for two-photon excitation yields the same results as Eqns. (21) and (22) but with $\langle I\rangle$ replaced by

$$\langle I^2\rangle = \bar{I}^2\delta t/T \tag{23}$$

and I_S' replaced by

$$I_S'' = (\eta'' T/\tau_F)^{-1}, \tag{24}$$

where

$$\eta'' = \sigma_{TPF}\tau_F/E_\gamma^2\ . \tag{25}$$

Eqns. (4), (17), and (22) may be approximated by power series expansions in $\langle I\rangle$ to yield

$$F = C\sum_{n=1}^{\infty}\alpha_n\left(\langle I\rangle/I_S\right)^n, \tag{26}$$

where

$$\alpha_n = -k_{10}(-1)^n/(1+Q), \quad \text{for cw excitation with } \langle I\rangle < I_S, \tag{27}$$

$$\alpha_n = -k_{10}(\tau_F/T)(-1)^n/n!, \quad \text{for sub-nanosecond pulsed excitation with } Q = 0,\ I_S \to I_S'. \tag{28}$$

$$\alpha_n = -k_{10}(\tau_F/2T)(-2)^n/n!, \quad \text{for sub-picosecond pulsed excitation with } Q = 0,\ I_S \to I_S',\ \text{or } I_S \to I_S''. \tag{29}$$

Fig. 2 illustrates the differences between Eqns. (4), (17), and (22) for the case of no triplet, $R = Q = 0$, and also a comparison with the Taylor expansions of Eqns. (26)—(29) in which only the first two terms are kept.

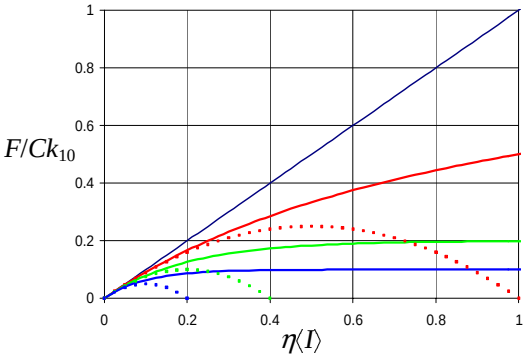

Fig. 2: F/Ck_{10} vs. $\eta\langle I\rangle$ as calculated by Eqn. (4) with Q=0 (red; top), and Eqns. (16) (green; middle) and (21) (blue; bottom) for T/τ_F = 5. The dashed curves show the corresponding Taylor expansions of Eqns. (26), (27), (28), and (29) with just the first two terms kept. Note that the signal rate at which excitation saturation occurs is lower for pulsed excitation than for cw excitation, and is lower still for two-photon excitation. For cw excitation, the first order Taylor approximation is adequate for $\eta\langle I\rangle < \sim 0.2$.

2. FLUORESCENCE PROFILE WITH SATURATION

For a Gaussian laser beam focused by a moderate N.A. microscope objective, the irradiance profile near the focus is

$$I(x,y,z)=\frac{2P}{\pi\omega_0^2\left(1+\left(z/z_0\right)^2\right)}\exp\left(\frac{-2\left(x^2+y^2\right)}{\omega_0^2\left(1+\left(z/z_0\right)^2\right)}\right), \tag{30}$$

where P is the laser power, ω_0 is the beam waist, the Rayleigh range is

$$z_0=n_0\pi\omega_0^2/\lambda_0, \tag{31}$$

n_0 is the refractive index of the solvent, and λ_0 is the vacuum wavelength of the laser. Moreover, for $z < z_0$

$$I(x,y,z)\approx\frac{2P}{\pi\omega_0^2}e^{-\frac{2(x^2+y^2)}{\omega_0^2}}\frac{1}{1+(z/z_0)^2}\approx\frac{P}{2\pi\sigma^2}e^{-\frac{(x^2+y^2)}{2\sigma^2}}e^{-\frac{z^2}{2\sigma_z^2}}=P\sqrt{2\pi}\sigma_z G(x,\sigma)G(y,\sigma)G(z,\sigma_z) \tag{32}$$

where

$$G(s,\sigma')=\frac{1}{\sqrt{2\pi}\sigma'}\exp\left(-\frac{s^2}{2\sigma'^2}\right) \tag{33}$$

denotes a Gaussian with standard deviation σ', normalized such that

$$\int_{-\infty}^{\infty}ds\,G(s,\sigma')=1, \tag{34}$$

and where we have set

$$\sigma=\omega_0/2 \quad\text{and}\quad \sigma_z=z_0/\sqrt{2\ln 2} \tag{35}$$

so that the half-width of the Lorentzian profile in z is matched to the half-width of the Gaussian approximation. Similarly, with $[1+(z/z_0)^2]^{-n}\approx G(z,\sigma_z/\sqrt{2^{1/n}-1})\sqrt{2\pi}\sigma_z/\sqrt{2^{1/n}-1}$, we have

$$I^n(x,y,z)\approx P^n(2\pi)^{3/2-n}n^{-1}\sigma^{2-2n}\sigma_z(2^{1/n}-1)^{-1/2}G(x,\sigma/\sqrt{n})G(y,\sigma/\sqrt{n})G(z,\sigma_z/\sqrt{2^{1/n}-1}). \tag{36}$$

The mean number of fluorescence photons per second detected from a single molecule located at x,y,z is given by Eqn. (4), (16), or (21) with $\langle I\rangle$ replaced by $I(x,y,z)$, which is approximated by the 3-D Gaussian profile of Eqn. (32), and with C replaced by the collection efficiency function $C(x,y,z)$, which is also approximated to be 3D-Gaussian in shape

$$C(x,y,z)=C_0\left(2\pi\right)^{3/2}\sigma_C^2\sigma_{Cz}G(x,\sigma_C)G(y,\sigma_C)G(z,\sigma_{Cz}), \tag{37}$$

with C_0 equal to the peak collection efficiency, and σ_C ,σ_{Cz} equal to the standard deviations in the radial and axial directions, as determined by the pinhole radius, and the magnification and numerical aperture of the microscope objective. Fig. 3 shows that as the laser irradiance increases, the fluorescence profile does not attain the flat-top profile that was assumed in Ref. [8] for $C(x,y,z) = 1$ and for the case of Eqn. (21) for two-photon sub-picosecond excitation.

Since the product of two Gaussian functions is another Gaussian,

$$G(s,\sigma_1)G(s,\sigma_2)=G(0,(\sigma_1^2+\sigma_2^2)^{1/2})G(s,(\sigma_1^{-2}+\sigma_2^{-2})^{-1/2}) \quad , \tag{38}$$

Eqn. (26) may be used to express the fluorescence profile as a sum of 3-D Gaussian functions:

$$F(x,y,z)=\sum_{n=1}^{\infty}\Phi_n G(x,\bar{\sigma}(n))G(y,\bar{\sigma}(n))G(z,\bar{\sigma}_z(n)), \tag{39}$$

where

$$\Phi_n=\left(\alpha_n/I_S^n\right)C_0P^n(2\pi)^{3/2-n}n^{-1}\sigma^{2-2n}(2^{1/n}-1)^{-1/2}\sigma_z\sigma_C^2\sigma_{Cz}(\sigma_C^2+\sigma^2/n)^{-1}(\sigma_{Cz}^2+\sigma_z^2/(2^{1/n}-1))^{-1/2}, \tag{40}$$

$$\bar{\sigma}(n)=\left(n\sigma^{-2}+\sigma_C^{-2}\right)^{-1/2}, \qquad \bar{\sigma}_z(n)=\left((2^{1/n}-1)\sigma_z^{-2}+\sigma_{Cz}^{-2}\right)^{-1/2}. \tag{41}$$

For low laser power and no saturation, only the first term in the sum of Eqn. (39) need be retained and the profile is 3-D Gaussian.

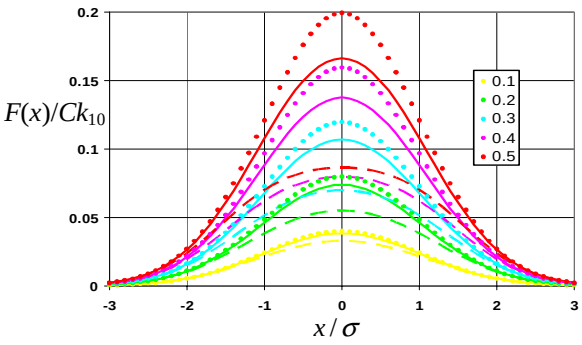

Fig. 3: Gaussian irradiance profiles with no saturation (dotted) and the resulting fluorescence profiles with saturation, obtained using Eqn. (4) for cw excitation (solid), and Eqn. (21) for sub-picosecond excitation for $T/\tau_F = 5$ (dashed). The profiles are for the cross-section at $y = z = 0$, with $I(x)/I_S = 0.1, 0.2, 0.3, 0.4, 0.5 \times G(x,\sigma)$. Note that the saturated profiles do not have the "flat-top" profile that was assumed in Ref. [8].

3. FORM OF THE AUTOCORRELATION FUNCTION WITHOUT SATURATION

The normalized ACF is defined as

$$g(\tau) = \frac{\langle F(t)F(t+\tau)\rangle}{\langle F(t)\rangle\langle F(t+\tau)\rangle}, \tag{42}$$

where $F(t)$ is the photon count rate at time t, and the angular brackets denote an average over all times, whereby

$$\langle F(t)F(t+\tau)\rangle = \lim_{T\to\infty} \frac{1}{2T}\int_{-T}^{T} F(t')F(t'+\tau)\,dt' \ . \tag{43}$$

A derivation of the theoretical form of $g(\tau)$ for the case of diffusion-induced concentration-fluctuations is given in the early FCS literature. Here we give a reformulated derivation in terms of single-photon detection from single-molecules, and the derivation is then extended to account for saturation. Let the number density of molecules be N molecules m^{-3}. Note that N also equals the probability density to find a single molecule at any location x,y,z. If $F(t)$ is a stationary ergodic random process, then the time averages in Eqn. (42) may be evaluated as ensemble averages and the average total rate of photons is independent of time and equals the count rate averaged over all possible molecule locations:

$$\langle F(t)\rangle = \iiint NF(x,y,z)dxdydz + B \tag{44}$$

$$= N\Phi + B, \tag{45}$$

where B is the total background count rate, and where we have retained only the first term of Eqn. (39), omitted the 1 notation in Φ_1, and used Eqn. (34) to perform the integrations. As $F(t)$ is a stationary random variable, each of the two factors in the denominator of Eqn. (42) is given by Eqn. (45). The term $F(t)\,F(t+\tau)$ in the numerator is the rate of detection of pairs of photons that are separated by an interval τ. The first photon may arise from a single-molecule located at x_1, y_1, z_1, with probability density N, or background. The second photon may arise either from the same single-molecule, which has moved from x_1, y_1, z_1, to x_2, y_2, z_2 during the time interval τ, with a probability density $M(x_1-x_2, y_1-y_2, z_1-z_2, \tau)$ or from a different single-molecule, again with probability density N, or from background. The numerator of Eqn. (42) is thus:

$$\begin{aligned}\langle F(t)F(t+\tau)\rangle = {} & \iiint dx_1dy_1dz_1NF(x_1,y_1,z_1)\iiint dx_2dy_2dz_2M(x_1-x_2,y_1-y_2,z_1-z_2,\tau)F(x_2,y_2,z_2) \\ & + \left[\iiint dx_1dy_1dz_1NF(x_1,y_1,z_1)\right]^2 + 2B\iiint dx_1dy_1dz_1NF(x_1,y_1,z_1) + B^2,\end{aligned} \tag{46}$$

where

$$M(x,y,z,\tau) = G(x,\sigma_D(\tau))G(y,\sigma_D(\tau))G(z,\sigma_D(\tau)) \tag{47}$$

is the probability density for a molecule to diffuse from the origin to x,y,z at time τ, and

$$\sigma_D(\tau) = \sqrt{2D\tau} \ . \tag{48}$$

Eqn. (47) is the solution of the diffusion equation

$$\partial N/\partial t = D\nabla^2 N \tag{49}$$

for the initial condition of a molecule located at the origin, $N(x,y,z,0) = \delta(0,0,0)$, where $\delta(x,y,z)$ is a 3-D Dirac delta function, and D is the diffusion coefficient. If there is a constant net flow component $\mathbf{v} = v_x, v_y, v_z$ throughout the probe volume, or if the sample is translated as in scanning FCS, then a term $-\mathbf{v}\cdot\nabla N$ is added to the right of Eqn. (49) and the Gaussian probability densities in Eqn. (47) become increasingly displaced from the origin with time so that

$$M(x,y,z,\tau) = G(x-v_x\tau,\sigma_D(\tau))G(y-v_y\tau,\sigma_D(\tau))G(z-v_z\tau,\sigma_D(\tau)) \ . \tag{50}$$

The integrations on the second line of Eqn. (46) are easily performed by use of Eqn. (34), as was done to obtain Eqn. (45) from (44), to yield $(N\Phi + B)^2$. For the first line, the integrations for each dimension may be performed separately. For the x-dimension, the integration is

$$I_x = \int dx_1 G(x_1,\bar{\sigma})\int dx_2 G(x_1-x_2-v_x\tau,\sigma_D(\tau))G(x_2,\bar{\sigma}) \ . \tag{51}$$

Note that the convolution of two Gaussians is another Gaussian, with a width that is the sum in quadrature of the widths of the two:

$$\int dx\, G(x,\sigma_1)G(x\pm x',\sigma_2) = G(x',\sqrt{\sigma_1^2+\sigma_2^2}). \tag{52}$$

Application of Eqn. (52) to Eqn. (51) yields

$$I_x = G\left(v_x\tau,\sqrt{2\bar{\sigma}^2+\sigma_D^2}\right) = G\left(\tau/\tau_F^{(x)},\sqrt{(1+\tau/\tau_D)/2}\right)\Big/\bar{\omega}_0, \tag{53}$$

where

$$\tau_F^{(x)} = \bar{\omega}_0/v_x, \quad \tau_D = \bar{\omega}_0^2/4D, \tag{54}$$

are the mean flow and diffusional residence times in the probe volume of a molecule that begins at the origin, and we have used $G(as,a\sigma) = G(s,\sigma)/a$, and from Eqn. (35) and Eqn. (41) with $n = 1$ denoted

$$\bar{\omega}_0 = 2\bar{\sigma} = 2\left(4\omega_0^{-2} + \sigma_C^{-2}\right)^{-1/2}, \quad \bar{z}_0 = 2\bar{\sigma}_z = 2\left(4z_0^{-2} + \sigma_{Cz}^{-2}\right)^{-1/2}. \tag{55}$$

For the *z*-dimension, the integration is

$$I_z = G\left(\tau/\tau_F^{(z)}, \sqrt{(1+(\bar{\omega}_0/\bar{z}_0)^2\tau/\tau_D)/2}\right)\Big/\bar{\omega}_0, \tag{56}$$

with

$$\tau_F^{(z)} = \bar{z}_0 / v_z. \tag{57}$$

Applying Eqns. (54) and (56) and $I_y = I_x$ in (46) yields

$$\langle F(t)F(t+\tau)\rangle = (N\Phi + B)^2 + \left(N\Phi^2/\bar{\omega}_0^2\bar{z}_0\right)G_xG_yG_z \tag{58}$$

where

$$G_xG_yG_z = G\left(\tau/\tau_F^{(x)}, \sqrt{(1+\tau/\tau_D)/2}\right)G\left(\tau/\tau_F^{(y)}, \sqrt{(1+\tau/\tau_D)/2}\right)G\left(\tau/\tau_F^{(z)}, \sqrt{(1+(\bar{\omega}_0/\bar{z}_0)^2\tau/\tau_D)/2}\right). \tag{59}$$

For no flow, the product of the three Gaussian factors gives the familiar Lorentzian ACF shape:

$$G_xG_yG_z(\mathbf{v}=0) = \pi^{-3/2}[1+\tau/\tau_D]^{-1}[1+(\bar{\omega}_0/\bar{z}_0)^2\tau/\tau_D]^{-1/2}. \tag{60}$$

Substitution of Eqns. (45) and (58) into Eqn. (42) yields the following expression for the unity-background-subtracted normalized ACF:

$$\bar{g}(\tau) = g(\tau) - 1 = \frac{1}{(1+B/(N\Phi))^2}\frac{G_xG_yG_z}{N\bar{\omega}_0^2\bar{z}_0}. \tag{61}$$

4. FORM OF THE AUTOCORRELATION FUNCTION WITH SATURATION

To model saturation, higher order terms from Eqn. (39) must be used in Eqns. (44) and (46). Eqn. (45) becomes

$$\langle F(t)\rangle = N\sum_{n=1}^{\infty}\Phi_n + B, \tag{62}$$

and Eqn. (58) becomes

$$\langle F(t)F(t+\tau)\rangle = \left(N\sum_{n=1}^{\infty}\Phi_n + B\right)^2 + \left(N/\bar{\omega}_0^2\bar{z}_0\right)\sum_{n=1}^{\infty}\sum_{m=1}^{\infty}\Phi_n\Phi_m G^{(n,m)}, \tag{63}$$

where

$$G^{(n,m)} = G_x^{(n,m)}G_y^{(n,m)}G_z^{(n,m)}, \tag{64}$$

$$G_{x|y}^{(n,m)} = G\left(v_{x|y}\tau, \sqrt{\bar{\sigma}^2(n)+\bar{\sigma}^2(m)+\sigma_D^2}\right) = G\left(\tau/\tau_F^{(x|y)}, \sqrt{\left(\bar{\sigma}^2(n)+\bar{\sigma}^2(m)\right)/\bar{\omega}_0^2 + \tau/(2\tau_D)}\right)\Big/\bar{\omega}_0, \tag{65}$$

$$G_z^{(n,m)} = G\left(v_z\tau, \sqrt{\bar{\sigma}_z^2(n)+\bar{\sigma}_z^2(m)+\sigma_D^2}\right) = G\left(\tau/\tau_F^{(z)}, \sqrt{\left(\bar{\sigma}_z^2(n)+\bar{\sigma}_z^2(m)\right)/\bar{z}_0^2 + (\bar{\omega}_0/\bar{z}_0)^2\tau/(2\tau_D)}\right)\Big/\bar{z}_0. \tag{66}$$

Substituting these results into Eqn. (42) yields

$$\bar{g}(\tau) = \frac{\left(N/\bar{\omega}_0^2\bar{z}_0\right)\sum\sum\Phi_n\Phi_m G^{(n,m)}}{\left(\sum N\Phi_n + B\right)^2}. \tag{67}$$

If only the first two lowest order terms are retained, the result is

$$\bar{g}(\tau) \approx \frac{\left(N/\bar{\omega}_0^2\bar{z}_0\right)\left(\Phi_1^2G^{(1,1)} + 2\Phi_1\Phi_2G^{(1,2)}\right)}{N^2(\Phi_1^2 + 2\Phi_1\Phi_2) + 2N\Phi_1B} = \frac{G^{(1,1)} + 2(\Phi_2/\Phi_1)G^{(1,2)}}{N\bar{\omega}_0^2\bar{z}_0(1+2\Phi_2/\Phi_1 + 2B/(N\Phi_1))} \tag{68}$$

where $G^{(1,1)}$ is given by Eqn. (59), and for no flow by Eqn. (60), and

$$G^{(1,2)} = G^2\left(\tau/\tau_F^{(x|y)}, \sqrt{\left(\bar{\sigma}^2(1)+\bar{\sigma}^2(2)\right)/\bar{\omega}_0^2 + \tau/(2\tau_D)}\right)G\left(\tau/\tau_F^{(z)}, \sqrt{\left(\bar{\sigma}_z^2(1)+\bar{\sigma}_z^2(2)\right)/\bar{z}_0^2 + (\bar{\omega}_0/\bar{z}_0)^2\tau/(2\tau_D)}\right)\Big/\bar{\omega}_0^2\bar{z}_0, \tag{69}$$

and for no flow,

$$G^{(1,2)}(\mathbf{v}=0) = \pi^{-3/2}[\xi + \tau/\tau_D]^{-1}[\xi_z + (\bar{\omega}_0/\bar{z}_0)^2\tau/\tau_D]^{-1/2}, \tag{70}$$

with

$$\xi = \frac{3\sigma_C^2 + 2\sigma^2}{4\sigma_C^2 + 2\sigma^2} \approx \frac{3}{4}, \quad \xi_z = \frac{3\sigma_{Cz}^2 + 2\sigma_z^2}{4\sigma_{Cz}^2 + 2\sigma_z^2} \approx \frac{3}{4}, \text{ for } \sigma_C \gg \sigma, \sigma_{Cz} \gg \sigma_z. \tag{71}$$

Eqn. (68) can be used as a fitting function for ACF data collected at laser powers where saturation begins to occur. No additional empirical parameters are needed if the laser power and beam characteristics can be measured and the saturation intensity I_S is calculated from Eqn. (6), or if Φ_2/Φ_1 is experimentally measured, as explained in section 6. The power dependence of the background *B* must also be measured and included in the analysis. A similar procedure can be followed to obtain the functional form of cross-correlation functions with saturation. For example, if the same laser beam and collection optics define the same probe region for two different detection systems, *a* and *b*, which may respond to different emission wavelength bands with peak collection efficiencies of C_0^a, C_0^b, and with backgrounds B^a, B^b, Eqn. (63) would be replaced by the cross-correlation

$$\langle F^a(t)F^b(t+\tau)\rangle = \left(N\sum_{n=1}^{\infty}\Phi_n^a + B^a\right)\left(N\sum_{n=1}^{\infty}\Phi_n^b + B^b\right) + \left(N/\bar{\omega}_0^2\bar{z}_0\right)\sum_{n=1}^{\infty}\sum_{m=1}^{\infty}\Phi_n^a\Phi_m^b G^{(n,m)}. \tag{72}$$

5. EXPERIMENTAL MEASUREMENTS

Fig. 4a presents experimental measurements of the mean fluorescence count rate versus laser power, normalized by the solution absorption at each wavelength used, for an 11.4 μM solution of Rhodamine B in water. For these experiments, the incoming laser beam considerably under-filled the microscope objective to ensure that the beam was not tightly focused in the sample and the fluorescence was collected only from the central region of the focused beam by use of a small pinhole as a spatial filter. Under these conditions, it should not be necessary to account for the spatial integrations of Eqn. (44) and the fluorescence count rates are expected to directly follow the shape of Eqn. (4) for continuous wave (cw) and Eqn. (19) for sub-nanosecond pulsed excitation. Fig. 4a, which shows results for 532 nm 70ps/76MHz pulsed excitation and 514 nm cw excitation, thereby illustrates one of the key points that the fluorescence rate at which excitation saturation occurs is lower for pulsed excitation than for cw excitation.

Fig. 4b presents a series of autocorrelation curves collected from a 1.14 nM solution of Rhodamine B in water with cw excitation at 514 nm. The major change apparent is that the amplitude decreases for increasing laser power due to excitation saturation. From Eqn. (61), one expects a decrease in ACF amplitude with increasing background B and hence a small (<~10%) correction for background has already been applied in the plots of Fig. 4b, by separately measuring the background rate from pure water and renormalizing the curves by a factor of $(1+ B / F)^2$, where F is the fluorescence count rate. Detector afterpulses were also calibrated and corrected for in the results of Fig. 4b. In addition to the decrease in amplitude as the laser power is increased, the width of the ACF is also found to increase slightly, consistent with Eqn. (68). However, other photophysical effects, such as triplet crossing and photobleaching may also contribute to the changes as the laser power is increased. Although these effects can also be included in a curve-fitting model, a more direct demonstration of the saturation model derived in section 4 would result if such effects were absent. Therefore, in section 6, results from a Monte Carlo simulation are used to demonstrate the application of the saturation model.

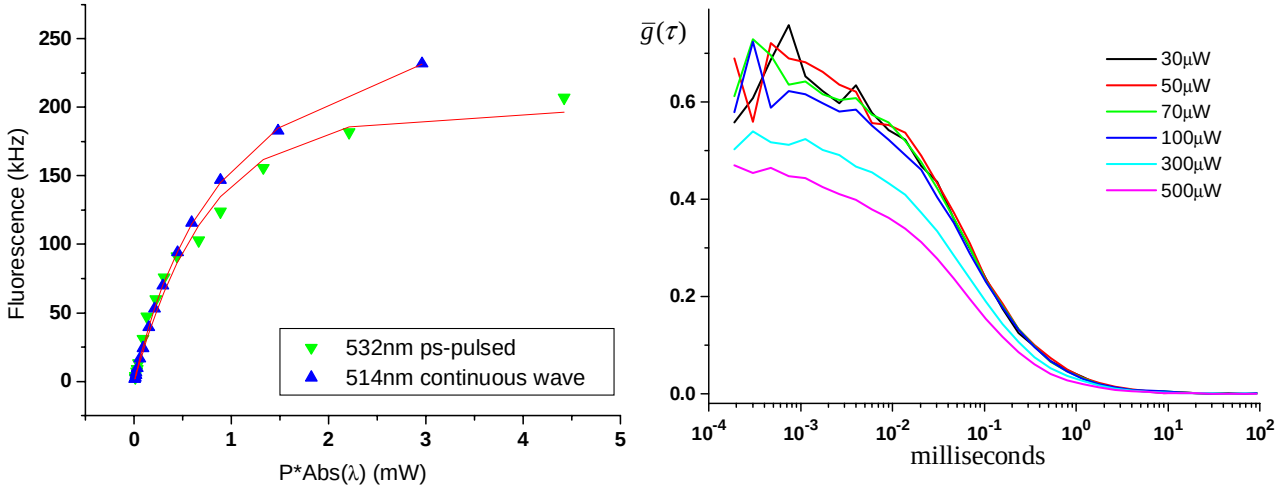

Fig. 4: (a) Experimental measurements of the fluorescence count rate versus laser power, normalized by the absorptivity at the used wavelength, illustrating differences in the onset of saturation for pulsed (532 nm) and continuous wave (514 nm) irradiation. The red curves are fits to Eqns. (19) and (4) respectively. (b) Measured autocorrelation function curves, after correction for background and afterpulses, for laser powers from 30 to 500 μW at the sample. As the laser power is increased, the ACF amplitude decreases, and the width increases slightly as the effective probe volume increases.

6. SIMULATED ACF DATA WITH SATURATION

An *ab-initio* Monte Carlo simulation of FCS for cw excitation [9] was used to generate ACF data for known experimental parameters, in order to demonstrate that curve fitting using Eqn. (68) can recover consistent parameters when saturation is present. The simulation models excitation saturation by requiring a time delay following each excitation of a molecule before subsequent excitation may occur, where the delay is a random real number with an exponential distribution with decay time equal to the fluorescence lifetime, or to the phosphorescence lifetime if triplet crossing occurs. Fig. 5a shows a series of ACF data generated by the simulation with background, triplet crossing, photobleaching, and solution flow set to zero, and with the pinhole opened so that $\sigma_C \gg \sigma, \sigma_{Cz} \gg \sigma_z$ to allow the

simplifications of Eqns. (71). Fig. 5b shows a plot of the total fluorescence count rate for this same set of data, together with a curve fit to a quadratic function

$$\langle F \rangle = aP + bP^2. \tag{73}$$

The total fluorescence is expected to follow Eqn. (62), and if only the first two terms are kept

$$\langle F \rangle \approx N(\Phi_1 + \Phi_2). \tag{74}$$

From Eqn. (40) it may be seen that

$$\Phi_1 \propto P, \quad \Phi_2 \propto P^2, \tag{75}$$

and hence, by comparing Eqns. (73) and (74),

$$\Phi_2/\Phi_1 = (b/a)P. \tag{76}$$

The ACF in Fig. 5a are fit to the standard "pure-diffusion" formula of Eqns. (60) and (61), and also, as shown in the figure, to the "saturation" model given by Eqns. (68), (60), and (70) using the measured value of Φ_2/Φ_1 determined from Fig. 5b and the known laser power, and with $\xi = \xi_z = 3/4$ in Eqn. (71). The 'confocal parameter' $(\bar{\omega}_0/\bar{z}_0)^2$ is held fixed so that there are two fitting parameters for each model. Fig. 6a shows that the decrease in amplitude of the ACF with increasing laser power is incorrectly interpreted by the pure-diffusion model as a change in the mean number of molecules in the probe volume, $\pi^{3/2} N \bar{\omega}_0^2 \bar{z}_0$, and Fig. 6b shows that the slight increase in width of the ACF with increasing laser power is incorrectly interpreted as an increase in the diffusional residence time, τ_D . By contrast, the "saturation" model gives consistent values as the laser power increases up to of ~250 μW. Beyond this point, a higher order approximation of Eqn. (67) with a cubic fit to Fig. 5b would be needed to achieve consistent parameter values.

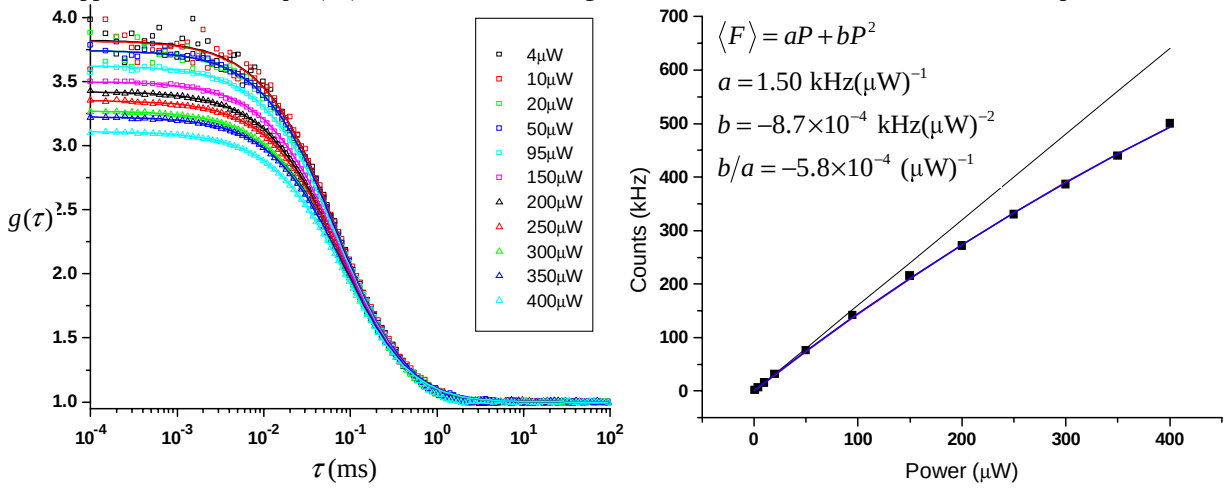

Fig. 5: (a) Series of simulated ACF for laser powers from 4 to 400 μW exhibiting changes due to excitation saturation; (b) the total fluorescence count rate versus laser power for the data in (a), together with a quadratic curve fit.

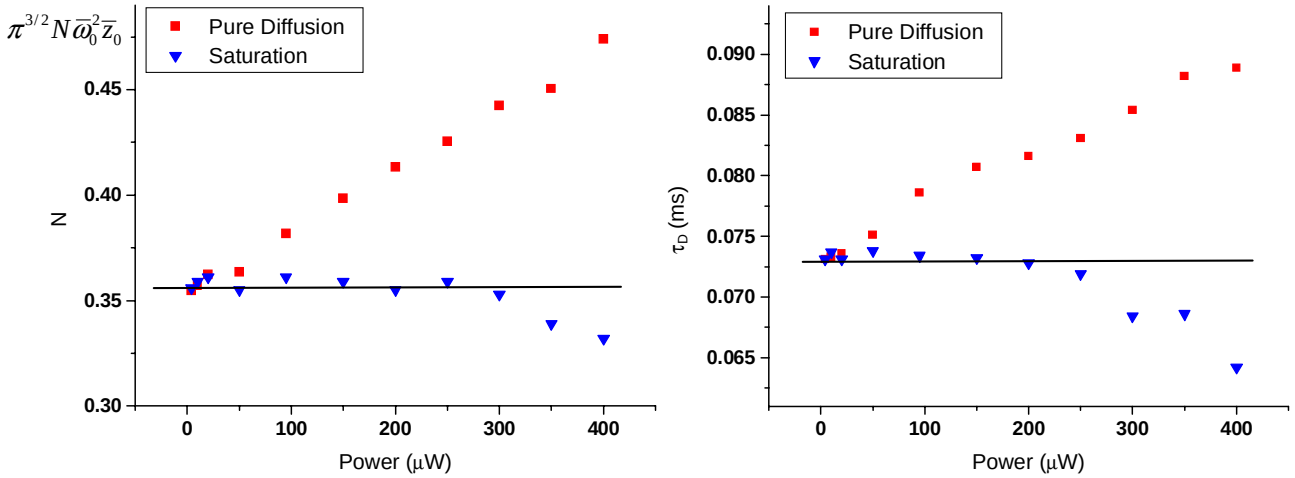

Fig. 6: The concentration (a), and the beam waist (b), calculated from the ACF fitting parameters results using the "pure diffusion" model of Eqns. (60) and (61), and the "saturation" model of Eqns. (68), (60), and (70) and the fit to Fig. 5b.

ACKNOWLEDGEMENTS

We thank Edmund D. Matayoshi and Kerry M. Swift of Abbott Laboratories for discussions leading up to this work.

REFERENCES

[1] *Fluorescence Correlation Spectroscopy: Theory and Applications*, R. Rigler and E.S. Elson, Eds., Springer, Berlin, 2001.
[2] "Dealing with reduced data acquisition times in fluorescence correlation spectroscopy (FCS) for high-throughput screening (HTS) applications," L.M. Davis, D.A. Ball, P.E. Williams, E.D. Matayoshi, and K.M. Swift, in *Microarrays and Combinatorial Technologies for Biomedical Applications*, D.V. Nicolau, and R. Raghavachari, Eds., Proc. SPIE **4966**, 117—128 (2003).
[3] "Systematic error in fluorescence correlation measurements identified by a simple saturation model of fluorescence," G. Nishimura and M. Kinjo, Anal. Chem. **76**, 1963 (2004).
[4] "Molecular photodynamics involved in multi-photon excitation fluorescence microscopy," J. Mertz, Eur. Phys. J. D **3**, 53—66 (1998).
[5] "Investigating two-photon photophysics with fluorescence correlation spectroscopy," K. Berland and G. Shen, in *Multiphoton Microscopy in the Biomedical Sciences III*, A. Perisamy, and P.T.C. So, Eds., Proc. SPIE **4963**, 1—12 (2003).
[6] "Excitation saturation in two-photon fluorescence correlation spectroscopy," K. Berland and G. Shen, Appl. Opt. **42**, 5566—5576 (2003).
[7] "Fluorescence correlation spectroscopy: incorporation of probe volume effects into the three-dimensional Gaussian approximation," M. Marrocco, Appl. Opt. 43, 5251—5262 (2004).
[8] "Saturation modified point spread functions in two-photon microscopy," G.C. Cianci, J. Wu and K.M. Berland, Microscopy Research and Technique **64**, 135—141 (2004).
[9] "Data reduction methods for application of fluorescence correlation spectroscopy to pharmaceutical drug discovery," L.M. Davis, P.E. Williams, D.A. Ball, E.D. Matayoshi, and K.M. Swift, Curr. Pharm. Biotech. **4**, 451—462 (2003).